Princeton Plasma Physics Laboratory

PPPL-5130

X-point Position Dependence of Edge Intrinsic Toroidal Rotation on TCV

T. Stoltzfus-Dueck, A. N. Karpushov, O. Sauter,
B. P. Duval, B. Labit, H. Reimerdes, W. A. J. Vijvers,
Y. Camenen, and the TCV Team

July 2015

Prepared for the U.S. Department of Energy under Contract DE-AC02-09CH11466.

Princeton Plasma Physics Laboratory
Report Disclaimers

Full Legal Disclaimer

This report was prepared as an account of work sponsored by an agency of the United States Government. Neither the United States Government nor any agency thereof, nor any of their employees, nor any of their contractors, subcontractors or their employees, makes any warranty, express or implied, or assumes any legal liability or responsibility for the accuracy, completeness, or any third party's use or the results of such use of any information, apparatus, product, or process disclosed, or represents that its use would not infringe privately owned rights. Reference herein to any specific commercial product, process, or service by trade name, trademark, manufacturer, or otherwise, does not necessarily constitute or imply its endorsement, recommendation, or favoring by the United States Government or any agency thereof or its contractors or subcontractors. The views and opinions of authors expressed herein do not necessarily state or reflect those of the United States Government or any agency thereof.

Trademark Disclaimer

Reference herein to any specific commercial product, process, or service by trade name, trademark, manufacturer, or otherwise, does not necessarily constitute or imply its endorsement, recommendation, or favoring by the United States Government or any agency thereof or its contractors or subcontractors.

PPPL Report Availability

Princeton Plasma Physics Laboratory:

http://www.pppl.gov/techreports.cfm

Office of Scientific and Technical Information (OSTI):

http://www.osti.gov/scitech/

Related Links:

U.S. Department of Energy

U.S. Department of Energy Office of Science

U.S. Department of Energy Office of Fusion Energy Sciences

X-point Position Dependence of Edge Intrinsic Toroidal Rotation on TCV

T. Stoltzfus-Dueck,[1] A. N. Karpushov,[2] O. Sauter,[2] B. P. Duval,[2] B. Labit,[2] H. Reimerdes,[2] W. A. J. Vijvers,[2] Y. Camenen,[3] and the TCV Team[2]

[1)] *Princeton University, Princeton, NJ 08544*

[2)] *École Polytechnique Fédérale de Lausanne (EPFL), Centre de Recherches en Physique des Plasmas (CRPP), CH-1015 Lausanne, Switzerland*

[3)] *Aix-Marseille Université, CNRS, PIIM UMR 7345, 13397 Marseille, France*

(Dated: February 25, 2015)

Recent theoretical work predicts intrinsic toroidal rotation in the tokamak edge to depend strongly on the normalized major radial position of the X-point, $\bar{R}_X$. With this motivation, we conducted a series of Ohmic L-mode shots on TCV, moving the X-point from the inboard to the outboard edge of the LCFS in both USN and LSN configurations. The edge toroidal rotation shifted strongly counter-current with increasing $\bar{R}_X$, either vanishing or changing sign to become counter-current for an outboard X-point, in agreement with the theoretical expectations. The whole rotation profile shifted roughly rigidly with the edge rotation, resulting in variation of the peak core rotation by more than a factor of 2. Core rotation reversals had little effect on the edge rotation. Edge rotation was slightly more counter-current for unfavorable than favorable ∇B discharges.

PACS numbers: 52.20.Dq, 52.25.Dg, 52.25.Fi, 52.25.Xz, 52.30.Gz, 52.35.We, 52.55.Dy, 52.55.Fa

I. INTRODUCTION

Toroidal rotation is important for the performance of fusion devices such as tokamaks and spherical torii, since it can stabilize the resistive wall mode[1] and its shear may sometimes suppress turbulent transport.[2] As ITER and future devices transition from neutral beam to alpha heating, the applied torque will become much smaller. For this reason, it is increasingly important to understand the physics underlying intrinsic rotation, the spontaneous toroidal rotation of the plasma in the absence of applied torque, which has been observed on many devices.[3,4] The boundary condition for any intrinsic rotation profile is set by the rotation in the edge region of the tokamak, meaning the steep normalized gradient region that extends a few cm minor radially on both sides of the last closed flux surface (LCFS). Intrinsic tokamak edge rotation is typically co-current and can be quite strong, reaching ion thermal Mach numbers of one to several tenths.[4–6] Dedicated experiments indicate that edge intrinsic toroidal velocities may be proportional to temperature or its gradient but independent of the density.[7,8]

Recent theoretical work has developed a simple kinetic transport model for intrinsic rotation in the tokamak edge, in which the spin-up follows from the interaction the different orbit excursions for co- and counter-current passing ions with the spatial variation of the turbulent viscosity.[9,10] For the model, momentum transport is assumed to be dominantly turbulent, as seen in experiment.[4,11] Since the turbulence is strong and the transport time is much longer than the turbulent decorrelation time,[12] the turbulent momentum transport is modeled by a simple viscosity. However, the amplitude of the transport-causing (unnormalized) turbulent potential fluctuations $\tilde{\phi}$, thus of the turbulent viscosity,[13] is allowed to vary spatially: poloidally in a general manner (usually taken outboard ballooning), and decaying with increasing minor radius r. [Probe measurements on many devices show that electron temperature T_e decays rapidly with increasing $r/a \gtrsim 0.85$ whereas normalized potential fluctuations $e\tilde{\phi}/T_e$ vary much less, such that the unnormalized $\tilde{\phi}$ decreases with increasing r.][14–23] The solution of the resulting transport equations, calculated in a two-region geometry with both a confined edge and a scrape-off layer (SOL),[9,10] shows that ions with differing parallel velocities are effectively diffused by an orbit-averaged turbulent viscosity that depends on the sign of their parallel velocity $v_\parallel$, as sketched in Fig. 1 of Ref. 24. For a typical configuration [Fig. 1(a) of Ref. 24], counter-current ions have a larger orbit-averaged viscosity and are therefore depleted from the plasma, resulting in co-current intrinsic rotation. For an atypical configuration with an outboard X-point [Fig. 1(b) of Ref. 24], the orbit-averaged viscosity becomes either equal or a bit larger for co- than counter-current ions, leading to vanishing or weakly counter-current intrinsic rotation.

In the simplest limit, the calculations of Refs. 9 and 10 yield an explicit formula for

$$v_{\rm pred} \approx 0.104\left(d_c/2 - \bar{R}_X\right)\frac{q}{L_\phi({\rm cm})}\frac{T_i({\rm eV})}{B_T({\rm T})}{\rm km/s}, \qquad (1)$$

roughly the flux-surface-averaged intrinsic toroidal rotation at the core-edge boundary, meaning the inner radial boundary of the steep gradient edge region, usually somewhere around $\rho\sim$0.85–0.9. In Eq. (1), $v_{\rm pred}$ is positive for co-current rotation, q is a representative edge safety factor, L_ϕ is the e-folding length for the minor-radial decay of $\langle\tilde{\phi}^2\rangle^{1/2}$, T_i is the ion temperature at the core-edge boundary, B_T is the toroidal field, and $\bar{R}_X \doteq [2R_X - (R_{\rm out} + R_{\rm in})]/(R_{\rm out} - R_{\rm in})$ indicates the normalized major radius of the X-point, going to -1 for an X-point at the high-field side (HFS) of the LCFS ($R_X \to R_{\rm in}$) and to +1 for an X-point at the low-field side (LFS) of the LCFS ($R_X \to R_{\rm out}$). The parameter d_c captures the poloidal variation of the turbulent viscosity, ranging from -2 to $+2$, with the latter indicating strongly outboard-ballooning transport (App. B). Eq. (1) captures many known features of edge intrinsic rotation: It is co-current for typical parameters ($d_c > 0$, $\bar{R}_X < 0$). It is proportional to $q/B_T \propto 1/I_p$, as in Rice scaling,[25] and to T_i, as seen in Refs. 7 and 8. It predicts a co-current spin-up at the L-H transition due to increasing T_i and decreasing L_ϕ.[4,26]

Eq. (1) predicts a strong linear dependence on $\bar{R}_X$, with rotation becoming more counter-current for an increasingly outboard X-point. Since $d_c/2\leq 1$, even for strongly outboard ballooning turbulence, $v_{\rm pred}$ either vanishes or becomes counter-current for an outboard enough X-point $\bar{R}_X \to +1$. With this motivation, we conducted a series of Ohmic L-

mode discharges on the Tokamak à Configuration Variable (TCV),[27] varying $\bar{R}_X$ over most of its possible range from -1 to +1, in both lower (LSN) and upper (USN) single null configurations. As we increased $\bar{R}_X$, the rotation at the core-edge boundary indeed shifted in the counter-current direction, shifting the whole rotation profile with it. The core-edge boundary rotation showed the expected linear dependence on $\bar{R}_X$ and became zero or counter-current for adequately outboard X-point. A fit of the observed rotation using Eq. (1) resulted in reasonable values for the two adjustable parameters d_c and L_ϕ. A modest counter-current shift for rotation in USN vs LSN discharges may indicate additional rotation drive beyond that in Eq. (1), or simply a geometric dependence of d_c or L_ϕ.

The rest of the paper is laid out as follows: In Sec. II we will discuss the experimental setup, parameter ranges, and time evolution of the discharges. Sec. III presents the principal results, focusing on observed rotation profiles and a detailed theory-experiment comparison. In Sec. IV, we will consider robustness of the observed behavior and the relation of the data with alternate theoretical pictures of intrinsic edge rotation. In Sec. V we will summarize the work, while some supporting theoretical calculations are deferred to Apps. A and B.

II. EXPERIMENTAL SETUP

TCV is a medium-sized tokamak (major radius R_0=88cm) with extreme geometric flexibility, which allowed us to achieve Ohmic L-mode plasma discharges with $\bar{R}_X$ ranging from near -1 to almost +1, in both LSN and USN configurations (Fig. 1). Most other plasma parameters were held fairly constant: minor radius $a \sim 22\,\mathrm{cm}$, average electron density $n_{e,\mathrm{avg}} \sim 1.4$–$2.2\times10^{13}\mathrm{cm}^{-3}$, and elongation $\kappa \sim 1.35$–1.45. The variation of $\bar{R}_X$ caused triangularity to vary from +0.4 down to −0.3. The plasma current I_p and "engineering" safety factor q_{eng} were around 150kA and 3.6–4 for most shots, but took somewhat different values ∼195kA and ∼3.0 for the two shots that exhibited a core rotation reversal.[28,29] All of the discharges were sawtoothing, which leads to a flattening of the core rotation profile inside the sawtooth inversion radius,[30] about $\rho \doteq (\psi/\psi_a)^{1/2} \sim 0.35$–$0.4$ for these shots.

Toroidal rotation and ion temperature were measured via charge-exchange (CXRS) on fully ionized carbon, using a relatively low current (1.67A) diagnostic neutral beam (DNBI).[31] The layout of beam and viewing chords (Fig. 2) allowed CXRS measurements on the HFS as well as the LFS, advantageous given the strong poloidal variation of toroidal rotation in the edge. The comparatively low ratio of active to passive emission necessitated background subtraction as described in Ref. 32, using the difference between total emission during the 20ms DNBI pulses and the linear interpolation of the passive emission measured during 40ms intervals before and after the beam pulse. The DNBI exerted negligible toroidal torque $\lesssim 10^{-4}\mathrm{N}\cdot\mathrm{m}$, about two orders of magnitude smaller than the theoretically estimated edge "intrinsic torque"[33]

$$\tau_{\mathrm{int}} \approx 1.38\cdot10^{-5}\left(\frac{1}{2}d_c - \bar{R}_X\right)\frac{q\,Q_i\,(\mathrm{kW})\,R_0\,(\mathrm{cm})}{L_\phi\,(\mathrm{cm})\,B_T\,(\mathrm{T})}\mathrm{N}\cdot\mathrm{m} \quad (2)$$

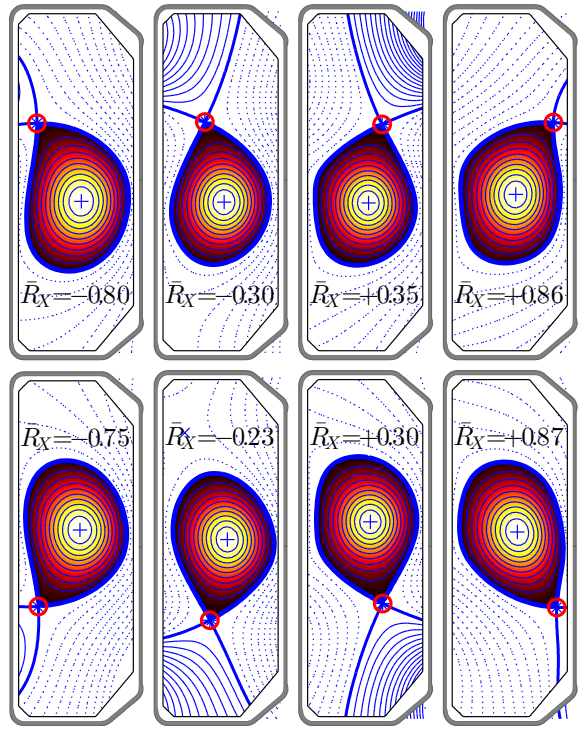

Figure 1. Representative plasma geometries, varying $\bar{R}_X$, in LSN (lower row) and USN (upper row) configurations.

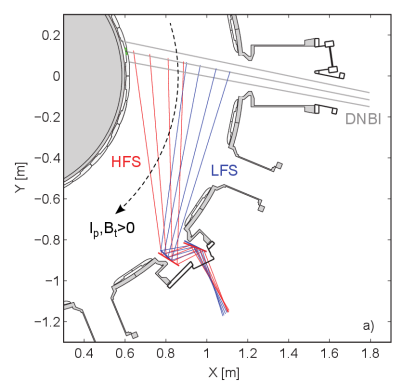

Figure 2. Top view of TCV, showing DNBI path and LFS and HFS CXRS viewing chords, as well as the positive direction for toroidal angle. *UPDATE FIGURE: i) Thicker lines, ii) I think the direction of positive toroidal angle is in fact backwards here?

expected for these plasmas, a few hundredths of a N · m. [In Eq. (2), Q_i is the ion heat flux in the edge.]

Fig. 3 shows the time evolution of a sample shot: After an initial limited phase, the X-point is pulled out of the inner wall before t=0.4s, held near the HFS until 0.6s, slowly ramped to a central radius over $0.6 \lesssim t \lesssim 1.0$s, then held there for the remainder of the shot. During the flat-top $t \geq$0.4s, in which I_p and the line-averaged density $n_{e,l}$ were feedback-controlled, the edge toroidal rotation on both the LFS and HFS (rolling-averaged over 3 subsequent CXRS measurements) decreased as $\bar{R}_X$ increased, settling at a weaker but still cocurrent rotation for the stationary $\bar{R}_X \approx -0.15$ phase. Other shot patterns included stationary X-points near the wall (HFS or LFS) as well as slow ramps of $\bar{R}_X$ over the entire flat-top period (from HFS or LFS wall). Data were taken for both static and sweeping X-point posi-

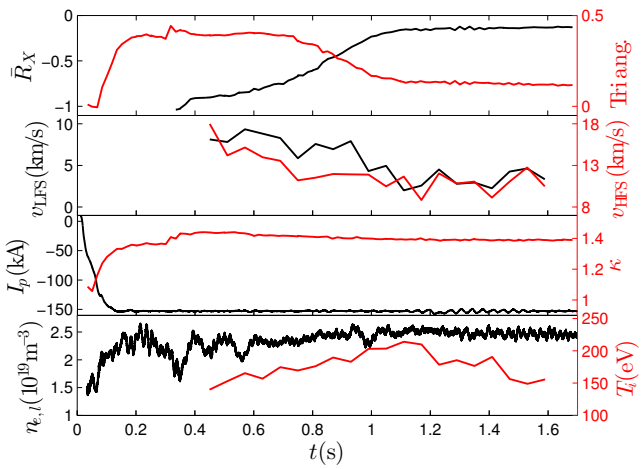

Figure 3. Time evolution of $\bar{R}_X$, triangularity, HFS and LFS toroidal velocities at $\rho = 0.85$, I_p, elongation κ, $n_{e,l}$, and T_i at $\rho = 0.85$.

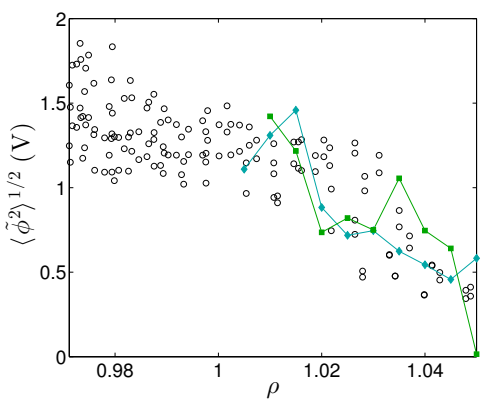

Figure 4. Radial profiles of the amplitude of floating potential fluctuations $\tilde{\phi}_{\rm fl}$ for shots 33349 (black circles, LSN/HFS X-point, reciprocating probe at outboard midplane), 48431 (green squares, LSN/HFS, wall-mounted probes), and 48433 (cyan diamonds, LSN/LFS, wall-mounted probes, scaled by a factor of 0.7).

tions, but the change of $\bar{R}_X$ was always small over the CXRS integration time.

The theoretical prediction $v_{\rm pred}$ depends on the radial decay length for unnormalized potential fluctuations L_ϕ. Althoughxs turbulence measurements were not a focus of the present experiments, wall-mounted Langmuir probe data allowed us to sample the fluctuating floating potential $\tilde{\phi}_{\rm fl}$ at the strikepoint with 5ms resolution, for a few shots. Higher-resolution (250 kHz) reciprocating Langmuir probe measurements of $\tilde{\phi}_{\rm fl}$ at the outboard midplane were available from an Ohmic L-mode shot (33349) from a previous campaign, but with similar plasma current and density. The radial profile of the $\tilde{\phi}_{\rm fl}$ amplitude from shot 33349 is compared with an LSN/HFS X-point shot (48431) and LSN/LFS X-point shot (48433) from the present campaign, with similar radial variation in all cases. Linear fits of the 33349 data, which extends into the confined plasma, lead to an estimate of L_ϕ∼3.5cm.

The theoretical prediction $v_{\rm pred}$ is a single value, thus must be compared with the experimentally measured velocity at some specific radial point. Roughly speaking, the mechanism underlying $v_{\rm pred}$ acts strongly at large $q\rho_i/L_\phi$, with ρ_i the ion gyroradius, so the comparison should be made at

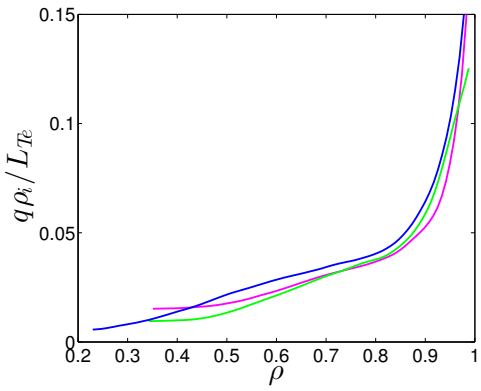

Figure 5. Radial profiles of $q\rho_i/L_{Te}$ for several shots, showing a steep radial increase starting around ρ∼0.85–0.9.

the radial boundary between small $q\rho_i/L_\phi$ (core) and large $q\rho_i/L_\phi$ (edge). Unfortunately, no fluctuating potential measurements within the confined plasma are available for the shots analyzed here. However, since $e\tilde{\phi}/T_e$ typically varies more weakly in r than T_e itself,[14–23] the quantity $q\rho_i/L_{Te}$ may be used as a reasonable proxy. As plotted in Fig. 5, $q\rho_i/L_{Te}$ increased slowly in the core $\rho \lesssim$0.85–0.9 and rapidly in the edge $\rho \gtrsim$0.85–0.9. Unfortunately, even $q\rho_i/L_{Te}$ is not well-determined for all shots, due to inadequate Thomson scattering data in the edge. From the theoretical side, the exact boundary in $q\rho_i/L_\phi$ is not precisely specified, and the correspondence between $q\rho_i/L_\phi$ and $q\rho_i/L_{Te}$ is not exact. Due to the resulting uncertainty in the best radial location for a theory-experiment comparison, in Sec. III we show results at a wide range of edge radial positions, finding the basic behavior to robustly hold at all of them.

III. RESULTS

The basic rotation behavior is exemplified by the radial profiles of the LFS and HFS carbon toroidal velocities for two shots, one with a stationary HFS X-point and one with a stationary LFS X-point (Fig. 6). The rotation at the core-edge boundary (around $\rho = 0.85$, circled in red) shifts strongly counter-current for the LFS X-point, by about 18km/s. The core rotation profiles ($\rho \lesssim 0.85$) shift fairly rigidly with the core-edge boundary condition—a large shift, more than doubling the peak rotation velocity. For comparison, Fig. 7 shows the same data as Fig. 6, but with the LFS X-point shot's data shifted rigidly in the co-current direction. The insensitivity of the core rotation profile gradient to such a large shift of the boundary condition suggests that the core rotation peaking drive in these shots is dominated by residual stress.

The theoretical prediction $v_{\rm pred}$ roughly represents a flux-surface-averaged toroidal velocity for deuterium. For a theory-experiment comparison, we approximated this with the LFS-HFS average of the measured toroidal velocity. We used the NEOART code[34,35] to neoclassically model the rotation difference between deuterium and carbon for four shots, one from each X-point quadrant (LSN/HFS, LSN/LFS, USN/HFS, and USN/LFS), finding the deuterium-carbon difference in the HFS/LFS-averaged toroidal rotation to be small (∼5km/s) and nearly constant across shots and

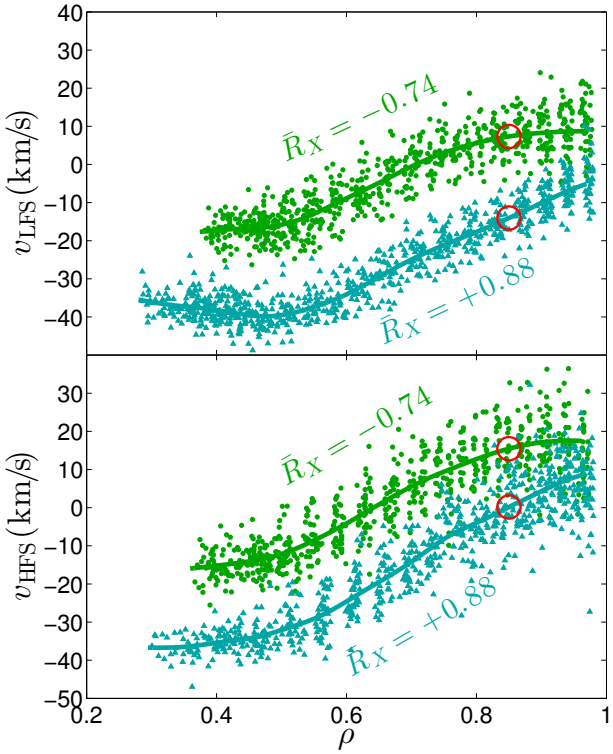

Figure 6. LFS and HFS carbon velocity measurement points (dots) and fitted profiles (lines) for an HFS ($\bar{R}_X$=−0.74) and LFS ($\bar{R}_X$=+0.88) X-point. The approximate core-edge boundary location $\rho = 0.85$ is marked with red circles. CXRS measurement error bars are comparable to point scatter.

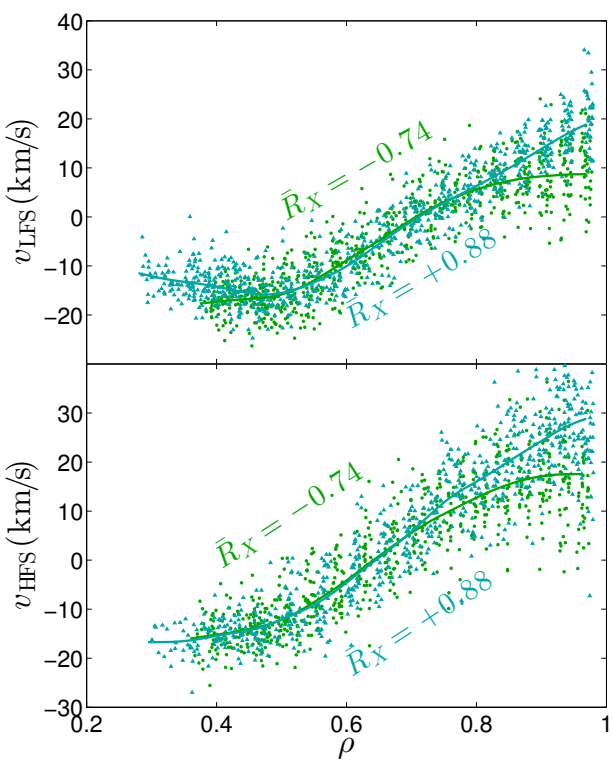

Figure 7. LFS and HFS carbon velocity measurement points (dots) and fitted profiles (lines) for an HFS ($\bar{R}_X = -0.74$) and LFS ($\bar{R}_X = +0.88$) X-point. The HFS X-point's rotation data has been shifted by +24km/s and +20km/s for the LFS and HFS profiles, respectively.

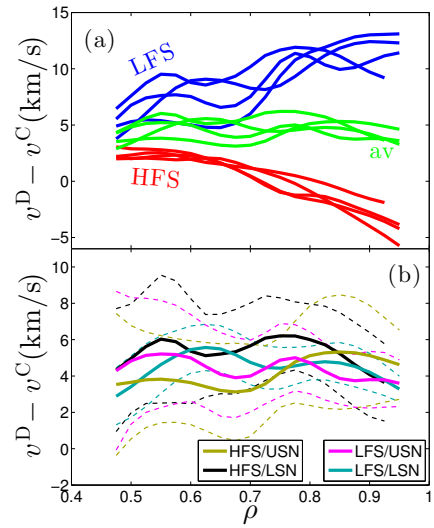

Figure 8. Neoclassical estimates of the deuterium-carbon toroidal velocity difference: (a) evaluated at the LFS, HFS, and with the LFS-HFS average (av), and (b) the LFS-HFS average with dashed error bars.

ρ, unlike either the LFS or HFS rotation on their own (Fig. 8). Defining $\Delta_{\rm C\to D}$ to be the deuterium-carbon LFS-HFS-averaged velocity shift, averaged over X-point quadrants, we therefore use

$$v_{0.85} \doteq \frac{1}{2}\left[v_{\rm LFS}\left(\rho = 0.85\right) + v_{\rm HFS}\left(\rho = 0.85\right)\right] + \Delta_{\rm C\to D}, \quad (3)$$

as well as the analogously defined $v_{0.80}$, $v_{0.90}$, and $v_{0.95}$, as estimates for the core-edge boundary rotation predicted by $v_{\rm pred}$. Small wall gaps and strong MHD modes caused significant rotation scatter, the latter also shifting rotation tendentially in the counter-current direction, so we filtered out measurement points with strong MHD modes, wall gaps <7mm, or CXRS error bars exceeding a threshold.[36] Unless otherwise noted, we exclude the two shots with a core rotation reversal from the following analysis and plots. We averaged all data over two adjacent CXRS measurements.

Fig. 9 shows $v_{0.80}$, $v_{0.85}$, $v_{0.90}$, and $v_{0.95}$ as functions of $\bar{R}_X$. At each radial position, the qualitative behavior is the same: a strong, approximately linear counter-current shift of the edge rotation as $\bar{R}_X$ increases, with rotation either vanishing or changing sign to become counter-current for large enough $\bar{R}_X$, in agreement with theoretical expectations. The rotation becomes modestly more co-current with increasing ρ, and is about 5.5km/s more counter-current for USN (unfavorable ∇B) than LSN (favorable ∇B) shots. The rms scatter about the fit, about 3.5km/s, is a little smaller than the measurement's average error bars, about 5km/s for ρ=0.80, 0.85, and 0.90 and about 10km/s for ρ=0.95.

The linear fits, combined with average values for $q_{\rm eng}$, T_i,[37] and B_T, allow us to infer values for the two unmeasured parameters d_c and L_ϕ, taken to be constants: $v_{0.80}$ yields d_c≈0.63 and L_ϕ≈4.7cm, $v_{0.85}$ yields d_c≈1.1 and L_ϕ≈4.3cm, $v_{0.90}$ yields d_c≈1.5 and L_ϕ≈3.8cm, and $v_{0.95}$ yields d_c≈1.9 and L_ϕ≈3.3cm. These values for L_ϕ are comparable to that inferred from the $\tilde{\phi}_{\rm fl}$ profiles in Fig. 4. Also, since the average L_{Te} was about 2.8cm, the inferred L_ϕ was about one to two times L_{Te}, placing L_ϕ/L_{Te} within the range observed in other experiments.[15–23] The fitted values for d_c indicate

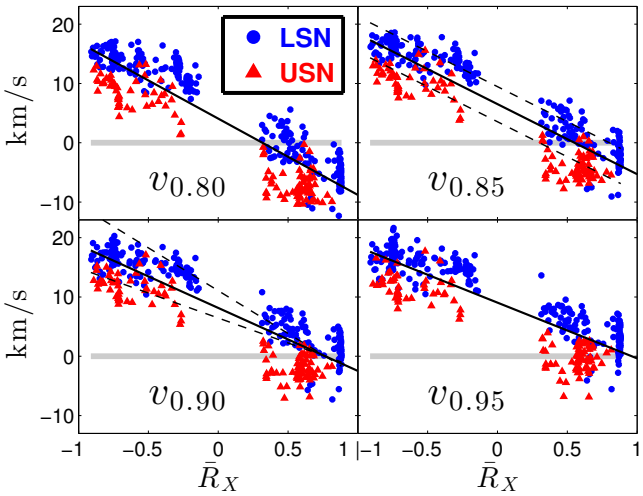

Figure 9. HFS-LFS averaged toroidal deuterium velocities at $\rho =$ 0.80, 0.85, 0.90, and 0.95, as functions of normalized major-radial X-point position $\bar{R}_X$. The dashed black lines for $v_{0.85}$ correspond to $d_c = 1.1 \pm 0.5$ and $L_\phi = 4.3$cm, those for $v_{0.90}$ correspond to $d_c = 1.5$, $L_\phi = 3.8 \pm 1$cm. Some mid-range $\bar{R}_X$ was inaccessible due to device constraints.

modestly (d_c≈0.63) to strongly (d_c≈1.9) outboard ballooning transport: as derived in App. B, the values d_c=0.63, 1.1, 1.5, and 1.9 respectively correspond to transport concentrated in the poloidal range $|\theta| \lesssim 135°$, 100°, 75° and 30° about the outboard midplane. To give a feel for the sensitivity of d_c and L_ϕ to the data, alternate fits are plotted for $v_{0.85}$ with d_c altered by ±0.5 and for $v_{0.90}$ with L_ϕ changed by ±1cm.

The edge rotation appeared to be fairly insensitive to the core rotation peaking. As a striking example, in two LSN shots an increased plasma current I_p ∼195kA triggered a reversal of the core rotation from its normal strong counter-current peaking to a weak co-current peaking, as has been previously observed on TCV.[28,30] Fig. 10 compares a normal and reversed rotation profile (both LSN with similar $\bar{R}_X$), showing that despite a change of nearly 40km/s in the core rotation, the shift in the edge rotation ($\rho \gtrsim 0.85$) was small ($\lesssim$5km/s). Fig. 11 shows that the core rotation reversal shifted the nominal core-edge rotation $v_{0.85}$ only marginally from the other LSN shots (∼+3.5km/s), while $v_{0.95}$ appears almost unaffected by the reversal (∼+1.7km/s).

From the profiles in Figs. 5 and 6, it is clear that the profile gradients just inside of $\rho = 0.85$ do in differ a bit between the HFS and LFS shots, albeit much less than the edge rotation itself varies. To examine this more closely, Fig. 12 shows the dependence of rotation increments inside the core plasma on both $v_{0.85}$ and on $\bar{R}_X$. Looking first at the rotation increments as functions of $v_{0.85}$, we see that the outer increments ($v_{0.80} - v_{0.90}$) and ($v_{0.70} - v_{0.80}$) depend weakly on $v_{0.85}$, while ($v_{0.60} - v_{0.70}$) and ($v_{0.50} - v_{0.60}$) show almost no dependence. Comparable plots of an increment as a function of the velocity at its outer edge, e. g. of ($v_{0.60} - v_{0.70}$) as a function of $v_{0.70}$, look almost the same as the increments as a function of $v_{0.85}$, presumably because the variation of the velocity at any radius is dominated by the variation of the edge rotation. Since the variation of the edge rotation is dominantly caused by variation of $\bar{R}_X$, we cannot empirically differentiate a dependence of the core rotation peaking on the edge rotation from a direct dependence of core peaking on the changing geometry. Indeed, the plots of rotation increments as functions of $\bar{R}_X$ show a gradual transition from a simple edge-rotation-like linear dependence on $\bar{R}_X$ for ($v_{0.80} - v_{0.90}$) to a "hump-like" structure for ($v_{0.50} - v_{0.60}$), with stronger peaking for $|\bar{R}_X| \to 1$ and weaker for $\bar{R}_X \to 0$. These plots are suggestive of a gradual transition from an edge-mechanism-dominated region for $\rho \gtrsim 0.8$ through an overlap region $0.7 \lesssim \rho \lesssim 0.8$ to a core-mechanism-dominated region for $\rho \lesssim 0.7$, but further investigation is needed.

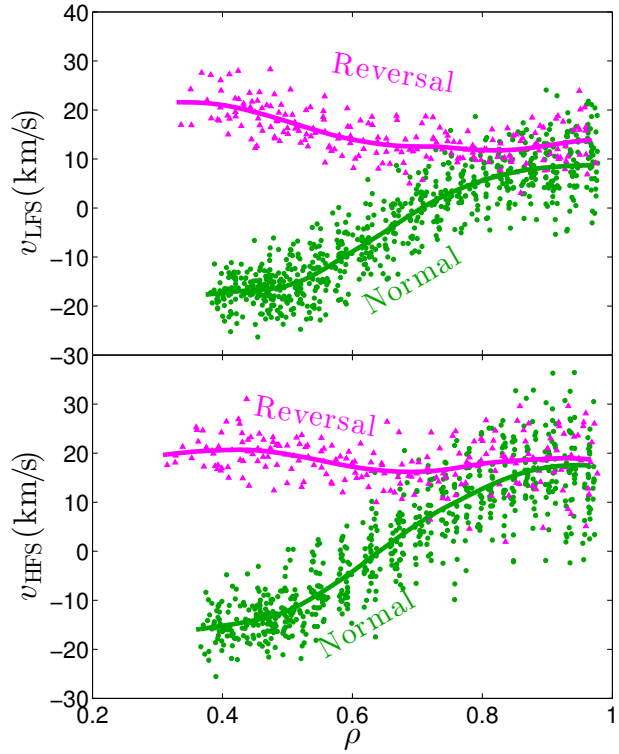

Figure 10. LFS and HFS carbon velocity measurement points (dots) and fitted profiles (lines) for a case with normal counter-current core rotation peaking and a case with a core rotation reversal.

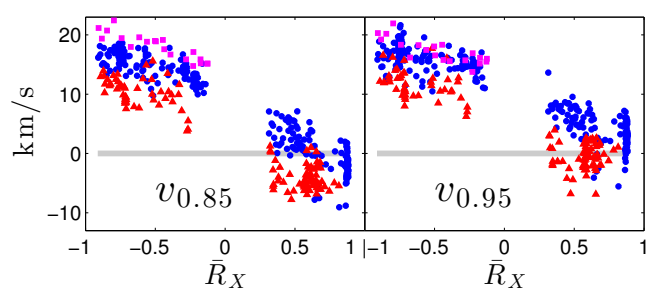

Figure 11. HFS-LFS averaged toroidal deuterium velocities at $\rho = 0.85$ and 0.95 as functions of $\bar{R}_X$, for LSN and USN with normal counter-current core rotation peaking (blue circles and red triangles respectively) and LSN with core rotation reversal (magenta squares).

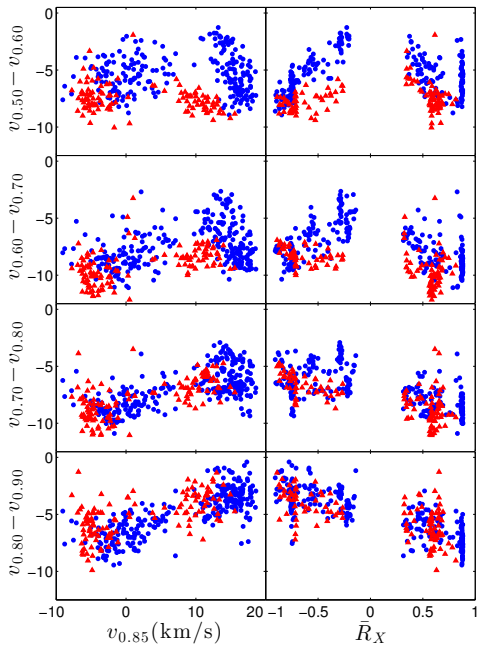

Figure 12. Rotation increments (in km/s) as functions of $v_{0.85}$ and $\bar{R}_X$.

IV. DISCUSSION

In this section, we will consider several aspects related to interpretation of the results of Sec. III: the choice of ρ for experiment-theory comparison, comparison of the experimental results with other theoretical pictures and physical mechanisms, relation of the experimental results with the structure of the theoretical problem, and possible future experiments motivated by the current results.

In the theoretical calculation underlying $v_{\rm pred}$,[10] the core rotation profile is flat and $v_{\rm pred}$ indicates the rotation at the center of the plasma. Physically, since the model contains only the edge rotation drive, this really corresponds to the rotation at the innermost boundary of the edge rotation mechanism, but outside of any core rotation peaking. However, typical TCV plasmas exhibit strong core rotation peaking (Fig. 6), while Fig. 12 suggests that there is an overlap region where both the core peaking mechanism (absent in the theory) and the edge rotation mechanism (included in the theory) are both active. This implies that there is no single radial location that is both inside the edge mechanism and outside the core peaking, preventing a perfect theory-experiment comparison. Fortunately, the variation of the boundary condition was much stronger than that of the core peaking (Figs. 6 and 12), allowing robust qualitative agreement between model and measurement over a wide range of ρ (Fig. 9).

The theoretical model underlying $v_{\rm pred}$ is simple, retaining a self-consistent combination of passing-ion orbit losses, momentum transport by spatially varying turbulent viscosity, two-region geometry (confined edge and SOL), and orbit-driven (∼Pfirsch-Schlueter) and transport-driven flows, but neglecting particle trapping, collisions and neoclassical transport, radial electric field shear, flux surface shaping, and nondiffusive turbulent momentum transport. These other physical effects could modify the mechanism or add other rotation drive terms, so we will briefly explore the bounds of the model underlying Eq. (1) and compare the data with other physical pictures or mechanisms.

Consider first the role of collisions. Neoclassical calculations typically predict weak momentum transport, much weaker than ion heat transport ($\chi_\phi \ll \chi_i$),[38] so experimental measurements showing comparable ion heat and momentum transport ($\chi_\phi \sim \chi_i$)[11,39–44] suggest that turbulence dominates the momentum transport channel. However, the dimensionless collisionality parameter $\nu_{ii}\tau_c$, roughly the number of collisions experienced by a thermal ion as it crosses the confined edge region, is a bit larger than 1 for the shots in this campaign, marginal values for applicability of the (collisionless) theory.[10,45] Although collisions conserve momentum, restricting their effect to some degree, they cause velocity-space scattering that makes ions "forget" their orbit displacements. Intuitively, this should blur the collisionless picture somewhat and quantitatively reduce the strength of the spin-up mechanism, but numerical simulations will be necessary to actually evaluate this effect.

The contribution of ion orbit losses to the edge intrinsic rotation has been previously considered.[7] Applied directly, the empty loss cone of the orbit loss picture predicts the in-out-averaged edge intrinsic rotation to become more *co*-current with increasing $\bar{R}_X$ for $\rho \lesssim 0.95$, in obvious disagreement with Fig. 9. However, the direct effect of ion orbit losses only extends a distance of order the poloidal gyroradius inside the separatrix, so ion orbit loss should really be coupled with momentum transport to construct a mechanism for intrinsic rotation further inside the confined plasma. In fact, Ref. 10 and the resulting Eq. (1) combines passing-ion orbit losses with transport, although trapped ions are neglected and the transport coefficient is assumed to decrease with r. One could attempt to isolate the contribution of orbit losses without radial variation of the diffusivity. As will be shown in an upcoming paper, if one does this with only passing ions, but with radially constant diffusivity, then such a calculation leads to a prediction resembling Eq. (1), but without the co-current offset $d_c/2$ due to the outboard ballooning transport. Since the measurements of Fig. 9 unambiguously indicate a co-current shift of the rotation, i.e. zero rotation occurs for $\bar{R}_X > 0$ regardless of ρ used for the comparison, the orbit loss picture without radial variation of the turbulence appears inconsistent with the data. As will be discussed in the upcoming paper, inclusion of trapped particles is also unable to bring the model to agreement with the data.

Transport-driven SOL flows have provided another physical picture for intrinsic rotation.[46] Basically, the idea is the following: Outboard ballooning transport leads to large parallel SOL flows away from the outboard midplane. At the inboard midplane, where these flows are strongest, they are co-current for favorable ∇B drift (LSN here) and counter-current for unfavorable ∇B drift (USN here). The inboard midplane flows then diffuse back into the plasma and cause a rotation increment in that direction. The signs one infers from this picture do indeed match with the slight counter-current shift observed for USN plasmas (Fig. 9). Interestingly, transport-driven SOL flow physics is included in the calculations of Ref. 10 and the expected strong inboard SOL flows are observed in the theoretical result, but the predicted intrinsic rotation at the boundary with the core does not change for USN relative to LSN configuration, if all other

input parameters are held constant. The theoretical reason for this is a symmetry about a "diffusion mid-point": if one integrates the momentum diffusivity poloidally starting at the X-point, and picks the poloidal angle at which half of the momentum diffusion has been completed, then that should be the null point in the transport-driven SOL flows. Flows go out from that point in both directions in the SOL, with equal diffusion remaining to bring them back in to the confined plasma, resulting in a cancellation.

One may also consider the transport-driven SOL flow model empirically: The transport-driven flows change sign upon a configuration change from LSN to USN, while Eq. (1) remains constant. The observed flows (Fig. 9) shift rather modestly in the counter-current direction, definitely not changing sign, thus are inconsistent with transport-driven SOL flows as a dominant drive for the edge rotation. Nevertheless, the small counter-current shift for USN shots remains unexplained. Perhaps some physics neglected in Ref. 10, such as particle sources and sinks in the bulk SOL,[47] could act on their own or interact with transport-driven flows to add this offset. On the other hand, it is possible that a LSN→USN configuration change simply changes the spatial structure of the turbulence somewhat, adjusting d_c and L_ϕ such that the rotation prediction $v_{\rm pred}$ shifts in the counter-current direction for unfavorable ∇B drift. This would require more strongly outboard ballooning turbulence for LSN than USN, e.g., if one fits $v_{0.85}$ separately for LSN and USN shots, one gets $L_\phi \approx 4.8$cm for both of them, with LSN $d_c \approx 1.42$ and USN $d_c \approx 0.46$ (transport respectively concentrated in $\pm 79°$ and $\pm 144°$ about the outboard midplane).

As plotted in Figs. 10 and 11, a core rotation reversal has almost no effect on the edge rotation, despite the large ~40km/s change in peak rotation. Surprising at first sight, this result emphasizes the structure of the steady-state edge rotation problem: momentum outflux through the edge must balance total torque τ applied to the core.[10] The momentum flux through the edge contains a residual stress R due to the orbit-shift effects (independent of toroidal velocity v at the core-edge boundary) and a viscous drag due to transport of bulk momentum out to the SOL $\propto \nu m n v$, with ν a turbulent viscosity. Setting the two momentum fluxes equal to the core torque determines the core-edge rotation velocity $v \propto (-R+\tau)/(mn\nu)$. Intrinsic rotation is the special case defined by vanishing torque $\tau \to 0$, so one balances the two momentum fluxes alone to get $v \propto -R/(mn\nu)$. Now, the core rotation reversal occurs entirely in the absence of applied torque: the residual stress in the core changes, so the velocity gradient in the core must change to maintain vanishing momentum flux, but all in the framework of toroidal momentum conservation with no applied torque. This means that τ stays zero for the edge problem in both the normal core peaking and rotation reversal case, so the core-edge rotation continues to relax to the value of vanishing total momentum flux $v \propto -R/(mn\nu)$ for both normal core peaking and rotation reversal, outside of any short-term transients during the transition.

One reasonable follow-up question is: how small must the core torque be to stay near intrinsic core-edge rotation? From the theory side, one expects that the core-edge rotation will stay near its intrinsic value if the core torque is small relative to the edge "intrinsic torque" $\tau_{\rm int}$ given by Eq. (2), which is just an estimate of $-R$ from the last paragraph. Indeed, the core-edge rotation is typically quite robust because it results from the balance between a large residual stress $R = -\tau_{\rm int}$ and a large viscous momentum outflux $\propto -\nu m \nabla(nv)$. The viscous momentum outflux can be quite large even if the edge velocity gradient is not that steep, because steep density gradients may cause the $v\nabla n$ term to dominate the momentum gradient $\nabla(nv)$. Note that this remains true even if the particle flux vanishes: Density and momentum solve different transport equations with different source terms (with a nonzero edge particle source but negligible momentum source) and with different transport coefficients. Since particle diffusivity D^p need not (and typically does not) equal turbulent viscosity ν, the momentum term $\nu m n v \nabla n$ does not need to equal mnv times the particle flux $D^p \nabla n$.

To close this section, we consider possible future experiments. Since $\bar{R}_X$ can strongly shift the rotation at the core-edge boundary, it changes the outer boundary condition for the core rotation profile and may therefore be useful in explorations of core rotation physics, for example to distinguish between pinch and residual stress mechanisms. However, it may be difficult to distinguish between effects of the changing core-edge rotation and effects of changing $\bar{R}_X$ itself (c.f. Fig. 12). The physics causing the $\bar{R}_X$-dependent rotation should also be active in H-mode, in fact even more strongly due to larger T_i and steeper gradients (smaller L_ϕ), so that one might be able to explore the role of rotation in the improved confinement. One could also attempt further tests of the model behind Eq. (1), for example by comparing edge rotation with detailed measurements of the $\tilde{\phi}$ amplitude profile to independently determine L_ϕ. One could also do joint scans of $\bar{R}_X$ and $I_p \propto q/B_T$ or T_i as a further parametric test of Eq. (1), although it may be difficult to vary I_p without changing other edge parameters like T_i or L_ϕ.

V. SUMMARY

A simple theoretical model for edge intrinsic rotation predicts a dependence of the edge toroidal rotation on the normalized X-point major radius $\bar{R}_X$, with rotation at the core-edge boundary predicted to shift strongly in the counter-current direction for increasing $\bar{R}_X$, either vanishing or becoming counter-current for a LFS X-point [Eq. (1)].[9,10] Motivated by this prediction, we performed a series of Ohmic L-mode discharges on TCV, scanning $\bar{R}_X$ over most of its possible range from -1 to +1 in both LSN (favorable ∇B) and USN configurations (Fig. 1). As $\bar{R}_X$ increased, the rotation at the core-edge boundary indeed shifted strongly in the counter-current direction, and the whole rotation profile shifted approximately rigidly with it, changing the core rotation velocity by more than a factor of two (Fig. 6). Examination of the measured toroidal velocity at several radial positions (ρ=0.80, 0.85, 0.90, 0.95) showed the expected qualitative dependence on $\bar{R}_X$, shifting from strong co-current rotation for the HFS X-point $\bar{R}_X \to -1$ to vanishing or counter-current rotation for an LFS X-point $\bar{R}_X \to +1$ (Fig. 9). Linear fits of the toroidal velocity as a function of $\bar{R}_X$ lead to reasonable values for the two constant inputs to the theory (d_c and L_ϕ), similar to values reported in the literature and values inferred from available measurements on TCV (Fig. 4). Rotation was modestly more counter-current for USN than LSN configurations. Core rotation reversals, acci-

dentally triggered in two shots, had little effect on the edge rotation (Figs. 10 and 11). Beyond its qualitative agreement the edge intrinsic rotation theory, the strong dependence of edge rotation on $\bar{R}_X$ may also be useful for future experiments investigating edge or core rotation or its impact on confinement.

ACKNOWLEDGMENTS

Helpful discussions with Jose Boedo, Rich Hawryluk, Per Helander, Josef Kamleitner, and Stewart Zweben are gratefully acknowledged. This work was supported in part by the Swiss National Science Foundation, the Max-Planck/Princeton Center for Plasma Physics, and the European Atomic Energy Community, with the work therefore subject to the provisions of the European Fusion Development Agreement.

Appendix A: Small-Diffusivity Calculation

Although the detailed calculations underlying Eq. (1) are quite complicated,[10] they may be greatly simplified in the limit of weak normalized turbulent viscosity $D \ll 1$, which often holds in practice. For example, in the present campaign $D \sim 10^{-2}$. As is typical, D is small despite the fact that the turbulent momentum transport is strong, simply because the normalization ($L_\phi^2 B_p v_{ti}/aB_T$, with B_p the poloidal field), is quite large $\sim 50\mathrm{m}^2/\mathrm{s}$.[48] In this Appendix, we will present a simplified small-D derivation of Eq. (1), which will serve as a basis for simplified calculations of a generalized system in App. B. Notation will follow that of Ref. 10, except for the substitution $\cos y_0 \to \bar{R}_X$.

The calculation begins with Eq. (1) of Ref. 10, with the same boundary conditions. After applying the variable transformations given in Sec. II of Ref. 10, one obtains Eq. (8) of Ref. 10,

$$\partial_{\bar{y}} f_i = \frac{1}{4} D_{\mathrm{eff}} \left(\partial_u^2 f_i - \frac{1}{u} \partial_u f_i \right), \tag{A1}$$

with boundary conditions as in Ref. 10. The key quantity of interest will be the radial flux of ions with a given normalized parallel velocity v, given in Eq. (11) of Ref. 10 as

$$\Gamma(v) = -\frac{1}{2} D_{y0} u^{-1} \int_0^1 \partial_u f_i \, d\bar{y} = -\frac{1}{2} D_{y0} u^{-1} \partial_u \bar{f}_i, \tag{A2}$$

in which $\bar{f}_i \doteq \int_0^1 f_i \, d\bar{y}$. For $u \leq 1$, Eq. (A1) has periodic boundary conditions in $\bar{y}$, so one may apply $\int_0^1 d\bar{y}$ to immediately solve for $\bar{f}_i = f_{i0} - c_q u^2$, where f_{i0} is the $u = 0$ boundary condition and c_q is an as-yet-unknown constant. Eq. (A2) then yields $\Gamma(v) = D_{y0} c_q$.

The actual calculation of c_q is quite complex, but for the case of weak diffusivity we may expect that the separatrix phase-space density $\bar{f}_i(u = 1)$ is much smaller than the core phase-space density $\bar{f}_i(u = 0)$, which implies $c_q \approx f_{i0}$, thus $\Gamma(v) \approx D_{y0} f_{i0}$. As shown in Fig. 13(a), the approximation $\Gamma \approx D_{y0} f_{i0}$ is fairly good for $D_{\mathrm{eff}} \lesssim 1/10$.

To compare the rotation prediction of this approximation with that of Ref. 10 Sec. V, we now assume $D(y) = D_0(1 + d_c \cos y)$ and $f_{i0}(v) = e^{-v^2/2}/\sqrt{2\pi}$ and take the first three v-moments of the small-D approximation to Γ, also showing the small-δ linearization [as is typical, $\delta \sim O(0.1)$ for the present experiments]:[49]

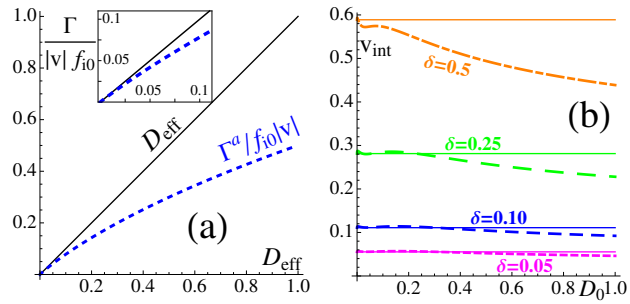

Figure 13. Normalized flux density $\Gamma/f_{i0}|v|$ (a) and intrinsic rotation velocity at core-edge boundary v_{int} (b), calculated for $d_c = 0.8$ and $\bar{R}_X \approx -0.71$ using the detailed calculation of Ref. 10 [thick broken lines, Γ^a (a) and Γ^ℓ (b)] and the small-D approximation of this appendix (thin solid lines).

$$\Gamma^p \approx \int_{-\infty}^{\infty} D_{y0} f_{i0} \, dv \overset{\delta \ll 1}{\approx} 2\pi D_0, \tag{A3a}$$

$$\Pi \approx \int_{-\infty}^{\infty} v D_{y0} f_{i0} \, dv \overset{\delta \ll 1}{\approx} -2\pi D_0 \delta \left(d_c/2 - \bar{R}_X \right), \tag{A3b}$$

$$Q_\parallel \approx \int_{-\infty}^{\infty} \frac{v^2}{2} D_{y0} f_{i0} \, dv \overset{\delta \ll 1}{\approx} \pi D_0. \tag{A3c}$$

The small-D prediction for the normalized intrinsic rotation velocity $v_{\mathrm{int}} = -\Pi/\Gamma^p$, compared with the prediction of Ref. 10 in Fig. 13(b), performs better than expected for moderate δ and D_0, primarily because the inaccuracies in Π and Γ^p roughly cancel in the ratio. Nevertheless, the principal purpose of this approximation is for the exploration of the case of non-sinusoidal diffusivity in App. B.

Appendix B: Non-Sinusoidal diffusivity

In Sec. V of Ref. 10, D was assumed vary sinusoidally with poloidal angle y, which led to the intrinsic rotation prediction v_{pred} given in Eq. (1), but with the outboard ballooning parameter d_c limited to the range $-1 \leq d_c \leq 1$. However, the turbulent transport may be more strongly localized to the outboard midplane than $\sin(y)$, which intuitively should lead to a larger range for d_c. In this Appendix, we check this by calculating the intrinsic rotation expected for turbulent transport concentrated into the poloidal angles $\pm y_d$ about the outboard midplane: $D(y) = D_0/2y_d$ for $|y| \leq y_d$ and 0 for $|y| \geq y_d$. We again follow the notation of Ref. 10 with the single modification $\cos y_0 \to \bar{R}_X$.

The calculations of Ref. 10 Sec. II may proceed unmodified for this case, with

$$D_{y0} = \frac{D_0}{2y_d} \int_{-y_d}^{y_d} e^{-\delta v (\cos y - \bar{R}_X)} dy \overset{\delta \ll 1}{\approx} D_0 e^{\delta v \bar{R}_X} \left(1 - s\delta v\right), \tag{B1}$$

with $s \doteq (\sin y_d)/y_d$. Following Sec. V of Ref. 10, taking $f_{i0} = e^{-v^2/2}/\sqrt{2\pi}$, and using $\Gamma \approx D_{y0} f_{i0}$ as in App. A for

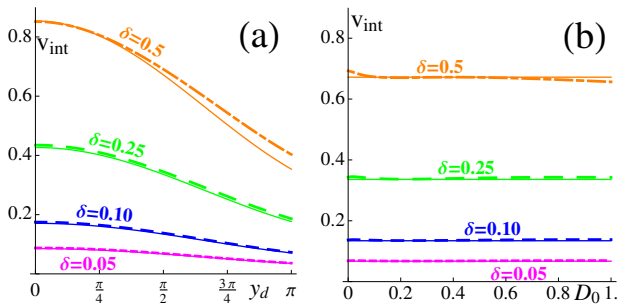

Figure 14. Normalized intrinsic rotation velocity at the core-edge boundary $v_{\rm int}$, calculated using the nonsinusoidal diffusivity for $\bar{R}_X \approx -0.71$ and various δ with: (a) $D_0 = 0.01$, scanning y_d, and (b) $y_d = \pi/2$, scanning D_0. Thick broken lines show the integral form using Γ^ℓ from Ref. 10 and D_{y0} from Eq. (B1) and thin solid lines show the small-D approximation from Eq. (B2).

the small-δ, D_0 expansion, one obtains

$$v_{\rm int} = -\frac{\int_{-\infty}^{\infty} v\Gamma\, dv}{\int_{-\infty}^{\infty} \Gamma\, dv} \overset{\delta, D_0 \ll 1}{\approx} \delta\left(s - \bar{R}_X\right). \qquad \text{(B2)}$$

Using $\bar{R}_X \approx -0.71$ (moderately HFS X-point), Fig. 14 plots $v_{\rm int}(y_d)$ at $D_0 = 0.01$ and $v_{\rm int}(D_0)$ at $y_d = \pi/2$, both for the integral representation [using $\Gamma = \Gamma^\ell$ from Eq. (42) of Ref. 10] and the explicit $\delta, D_0 \ll 1$ approximation of Eq. (B2). The simple small-D_0 expansion again performs much better than expected, due to the similar variation of Γ^p and Π with D_0.

Comparing Eq. (B2) with the analogous sinusoidal-D prediction, $-\Pi/\Gamma^p$ from Eqs. (A3), we see that the nonsinusoidal result is altered by the simple substitution $d_c/2 \to s$. The function s varies from 0 for $y_d = \pi$ (poloidally uniform D) to 1 for $y_d \to 0$ (D delta-concentrated at the outboard midplane), showing that d_c may in general vary up to $+2$. Conversely, we could have done an analogous calculation with D concentrated in a range about the inboard midplane, via which we would have obtained d_c down to -2. This makes physical sense: Recalling the orbit shift cartoon, as sketched in Fig. 1 of Ref. 24, consider the case with transport delta-function concentrated at the outboard midplane. In this case, only the orbit shifts exactly at the outboard midplane are relevant for determination of the rotation. Since that point is at the outermost edge of the flux surface, the rotation will always be co-current, going to zero as $\bar{R}_X \to +1$, as predicted by this formula.

REFERENCES

[1] E. Strait, T. S. Taylor, A. D. Turnbull, J. R. Ferron, L. L. Lao, B. Rice, O. Sauter, S. J. Thompson, and D. Wróblewski, Phys. Rev. Lett. **74**, 2483 (1995).

[2] H. Biglari, P. H. Diamond, and P. W. Terry, Phys. Fluids B **2**, 1 (1990).

[3] I. H. Hutchinson, J. E. Rice, R. S. Granetz, and J. A. Snipes, Phys. Rev. Lett. **84**, 3330 (2000).

[4] J. S. deGrassie, Plasma Phys. Controlled Fusion **51**, 124047 (2009).

[5] J.-M. Noterdaeme, E. Righi, V. Chan, J. deGrassie, K. Kirov, M. Mantsinen, M. F. F. Nave, D. Testa, K.-D. Zastrow, R. Budny, *et al.*, Nucl. Fusion **43**, 274 (2003).

[6] A. Bortolon, *Plasma Rotation and Momentum Transport Studies in the TCV Tokamak Based on Charge Exchange Spectroscopy Measurements*, Ph.D. thesis, École Polytechnique Fédérale de Lausanne (2009).

[7] J. S. deGrassie, R. J. Groebner, K. H. Burrell, and W. M. Solomon, Nucl. Fusion **49**, 085020 (2009).

[8] J. E. Rice, J. W. Hughes, P. H. Diamond, Y. Kosuga, Y. A. Podpaly, M. L. Reinke, M. J. Greenwald, Ö. D. Gürcan, T. S. Hahm, A. E. Hubbard, E. S. Marmar, C. J. McDevitt, and D. G. Whyte, Phys. Rev. Lett. **106**, 215001 (2011).

[9] T. Stoltzfus-Dueck, Phys. Rev. Lett. **108**, 065002 (2012).

[10] T. Stoltzfus-Dueck, Phys. Plasmas **19**, 055908 (2012).

[11] W. D. Lee, J. E. Rice, E. S. Marmar, M. J. Greenwald, I. H. Hutchinson, and J. A. Snipes, Phys. Rev. Lett. **91**, 205003 (2003).

[12] This follows from the steepness of edge gradients: The turbulent decorrelation rate goes as $k_\perp \tilde{v}_E \sim k_\perp v_{ti}/k_\perp L_\perp \sim v_{ti}/L_\perp$, in which v_{ti} is the ion thermal velocity and $L_\perp$ is the scale length for radial decay of plasma parameters (density, temperature), a cm or so in the edge. In near SOL, the turbulent transport divergence must balance the parallel losses to the sheath, thus it is of order $v_{ti}/L_\parallel$, where $L_\parallel$ is the parallel connection length, usually many meters. By continuity, the turbulent transport is of the same order in the outer edge as in the near SOL. So, for both outer confined edge and near SOL, the ratio of turbulent transport rate to decorrelation rate goes as $L_\perp/L_\parallel \ll 1$.

[13] Since the turbulence is strong, one may estimate the turbulent viscosity as $\tilde{v}_{E,r}^2 \tau_{ac} \sim \tilde{v}_{E,r}^2/k_\perp \tilde{v}_{E,r} \sim c\tilde{\phi}/B$, in which $\tilde{\phi}$ is the dimensional, unnormalized amplitude of potential fluctuations.

[14] C. P. Ritz, H. Lin, T. L. Rhodes, and A. J. Wootton, Rev. Lett. **65**, 2543 (1990).

[15] S. J. Zweben and R. W. Gould, Nucl. Fusion **25**, 171 (1985).

[16] M. Endler, H. Niedermeyer, L. Giannone, E. Holzhauer, A. Rudyi, G. Theimer, N. Tsois, and ASDEX Team, Nucl. Fusion **35**, 1307 (1995).

[17] R. A. Moyer, J. W. Cuthbertson, T. E. Evans, G. D. Porter, and J. G. Watkins, J. Nucl. Mater. **241–243**, 633 (1997).

[18] R. A. Moyer, R. Lehmer, J. A. Boedo, J. G. Watkins, X. Xu, J. R. Myra, R. Cohen, D. A. D'Ippolito, T. W. Petrie, and M. J. Schaffer, J. Nucl. Mater. **266–269**, 1145 (1999).

[19] J. Bleuel, M. Endler, H. Niedermeyer, M. Schubert, H. Thomsen, and the W7-AS Team, New J. Phys. **4**, 38 (2002).

[20] C. Silva, B. Gonçalves, C. Hidalgo, M. A. Pedrosa, K. Erents, G. Matthews, and R. A. Pitts, Rev. Sci. Instrum. **75**, 4314 (2004).

[21] B. LaBombard, J. W. Hughes, D. Mossessian, M. Greenwald, B. Lipschultz, J. L. Terry, and the Alcator C-Mod Team, Nucl. Fusion **45**, 1658 (2005).

[22] J. Horacek, J. Adamek, H. W. Müller, J. Seidl, A. H. Nielsen, V. Rohde, F. Mehlmann, C. Ionita, E. Havlíčková, and the ASDEX Upgrade Team, Nucl. Fusion **50**, 105001 (2010).

[23] J. A. Boedo *et al.*, Phys. Plasmas **21**, 042309 (2014).

[24] T. Stoltzfus-Dueck, A. N. Karpushov, O. Sauter, B. P. Duval, H. Reimerdes, W. A. J. Vijvers, Y. Camenen, and the TCV Team, Submitted to *Phys. Rev. Lett.*

[25] J. E. Rice *et al.*, Nucl. Fusion **39**, 1175 (1999).

[26] J. E. Rice, A. Ince-Cushman, J. S. deGrassie, L.-G. Eriksson, Y. Sakamoto, A. Scarabosio, A. Bortolon, K. H. Burrell, B. P. Duval, C. Fenzi-Bonizec, *et al.*, Nucl. Fusion **47**, 1618 (2007).

[27] S. Coda for the TCV team, Submitted to Nucl. Fusion.

[28] A. Bortolon, B. P. Duval, A. Pochelon, and A. Scarabosio, Phys. Rev. Lett. **97**, 235003 (2006).

[29] One of the two reversal shots had $n_{e,\rm avg} \sim 2.75 \times 10^{13}{\rm cm}^{-3}$.

[30] O. Sauter *et al.*, in *Fusion Energy Conference 2010 Book of Abstracts* (IAEA, 2010) p. 180.

[31] A. Karpushov, Y. Andrebe, B. P. Duval, and A. Bortolon, Fusion Engineering and Design **84**, 993 (2009).

[32] B. P. Duval *et al.*, Plasma Phys. Controlled Fusion **49**, B195 (2007).

[33] Eq. (2) is obtained from the dimensional forms of Eqs. (43) of Ref. 10, with $-\Pi$ the "intrinsic torque" and $(Q_\parallel + m_i v_{ti}^2 \Gamma^p)$ the ion heat flux.

[34] A. G. Peeters, Phys. Plasmas **7**, 268 (2000).

[35] A. Bortolon *et al.*, Nucl. Fusion **53**, 023002 (2013).

[36] Quantitative thresholds were chosen to be the parameter values for which the standard deviation of $v_{\rm exp} - v_{\rm pred}$ began to significantly exceed the standard deviation over the entire range of that parameter. About 13.9% of data was discarded due to MHD and about 9.8% due to small wall gaps or poor CXRS quality.

[37] In each case, T_i is evaluated at the same ρ as the toroidal velocity.

[38] F. L. Hinton and S. K. Wong, Phys. Fluids **28**, 3082 (1985).

[39] S. D. Scott, P. H. Diamond, R. J. Fonck, R. J. Goldston, R. B. Howell, K. P. Jaehnig, G. Schilling, E. J. Synakowski, M. C. Zarnstorff, C. E. Bush, *et al.*, Phys. Rev. Lett. **64**, 531 (1990).

[40] A. Kallenbach, H. M. Mayer, G. Fussmann, V. Mertens, U. Stroth, O. Vollmer, and the ASDEX Team, Plasma Phys. Controlled Fusion **33**, 595 (1991).

[41] J. E. Rice *et al.*, Nucl. Fusion **38**, 75 (1998).

[42] J. S. deGrassie, D. R. Baker, K. H. Burrell, P. Gohil, C. M. Greenfield, R. J. Groebner, and D. M. Thomas, Nucl. Fusion **43**, 142 (2003).

[43] J. E. Rice, W. D. Lee, E. S. Marmar, N. P. Basse, P. T. Bonoli, M. J. Greenwald, A. E. Hubbard, J. W. Hughes, I. H. Hutchinson, A. Ince-Cushman, *et al.*, Phys. Plasmas **11**, 2427 (2004).

[44] J. E. Rice, W. D. Lee, E. S. Marmar, P. T. Bonoli, R. S. Granetz, M. J. Greenwald, A. E. Hubbard, I. H. Hutchinson, J. H. Irby, Y. Lin, D. Mossessian, J. A. Snipes, S. M. Wolfe, and S. J. Wukitch, Nucl. Fusion **44**, 379 (2004).

[45] The theoretical model extends to $\nu_{ii}\tau_c$ somewhat larger than unity, because the parameter $\nu_{ii}\tau_c$ is evaluated for thermal ions, while the momentum is mostly carried by modestly superthermal ions, which are less collisional. See Fig. 5 of Ref. 10.

[46] B. LaBombard, J. E. Rice, A. E. Hubbard, J. W. Hughes, M. Greenwald, J. Irby, Y. Lin, B. Lipschultz, E. S. Marmar, C. S. Pitcher, N. Smick, S. M. Wolfe, S. J. Wukitch, and the Alcator Group, Nucl. Fusion **44**, 1047 (2004).

[47] P. Helander, T. Fülöp, and P. J. Catto, Phys. Plasmas **10**, 4396 (2003).

[48] To estimate D, we may evaluate the theoretically predicted dimensional heat flux $(Q_\parallel + T_i\Gamma^p)$ using Eqs. (43) and adjacent text of Ref. 10. In the limit $D \ll 1$, assuming deuterium (otherwise multiply by $\sqrt{\mu_i/2}$), this relation is easily inverted to give

$$D \approx 32.3 \frac{q\, Q_i(\mathrm{kW})}{n_i\,(10^{19}\mathrm{m}^{-3})\, T_i^{3/2}(\mathrm{eV}) L_\phi(\mathrm{cm}) a(\mathrm{cm})},$$

with T_i, Q_i, and ion density n_i all evaluated at the radial position of the core-edge boundary.

[49] The integral forms (resp. $\delta \ll 1$ forms) given here are the $D_0 \to 0$ (resp. $D_0, \delta \to 0$) limits of the integral forms of Eqs. (43) in Ref. 10. Further approximations necessary for the explicit small-δ forms in Ref. 10 cause some difference with the small-δ linearizations given here, although evaluation of v_{int} using those forms is quite accurate.

Princeton Plasma Physics Laboratory
Office of Reports and Publications

Managed by
Princeton University

under contract with the
U.S. Department of Energy
(DE-AC02-09CH11466)

P.O. Box 451, Princeton, NJ 08543
Phone: 609-243-2245
Fax: 609-243-2751

E-mail: publications@pppl.gov

Website: http://www.pppl.gov